

**Spatio-temporal
impact of convection:
methodology**

M. S. Johnston et al.

This discussion paper is/has been under review for the journal Atmospheric Chemistry and Physics (ACP). Please refer to the corresponding final paper in ACP if available.

Diagnosing the average spatio-temporal impact of convective systems – Part 1: A methodology for evaluating climate models

M. S. Johnston^{1,4}, P. Eriksson¹, S. Eliasson², M. D. Zelinka³, R. M. Forbes⁵, and K. Wyser⁴

¹Department of Earth and Space Sciences, Chalmers University of Technology, Göteborg, Sweden

²Department of Computer Science, Electrical and Space Engineering, Division of Space Technology, Luleå University of Technology, Kiruna, Sweden

³Program for Climate Model Diagnosis and Intercomparison, Lawrence Livermore National Laboratory, Livermore, California, USA

⁴Swedish Meteorological and Hydrological Institute, Norrköping, Sweden

⁵European Centre for Medium-Range Weather Forecasts, Reading, England

Received: 21 March 2013 – Accepted: 22 April 2013 – Published: 23 May 2013

Correspondence to: M. S. Johnston (marston@chalmers.se)

Published by Copernicus Publications on behalf of the European Geosciences Union.

Title Page

Abstract

Introduction

Conclusions

References

Tables

Figures

⏪

⏩

◀

▶

Back

Close

Full Screen / Esc

Printer-friendly Version

Interactive Discussion



Abstract

A method to determine the mean response of upper tropospheric water to localised deep convective (DC) events is improved and applied to the EC-Earth climate model. Following Zelinka and Hartmann (2009), several fields related to moist processes and radiation are composited with respect to local maxima in rain rate to determine their spatio-temporal evolution with deep convection in the central Pacific Ocean.

Major improvements to the above study are the isolation of DC events in time so as to prevent multiple sampling of the same event, and a revised definition of the mean background state that allows for better characterization of the DC-induced anomalies.

The DC events observed in this study propagate westward at $\sim 4 \text{ ms}^{-1}$. Both the upper tropospheric relative humidity and outgoing longwave radiation are substantially perturbed over a broad horizontal extent during peak convection and for long periods of time. Cloud fraction anomaly increases throughout the upper troposphere, especially in the 200–250 hPa layer, reaching peak coverage following deep convection. Cloud ice water content anomaly confined to pressures greater than about 250 hPa and peaks near 450 hPa within a few hours of the DC event but remain enhanced following the DC event. Consistent with the large increase in upper tropospheric cloud ice, albedo increases dramatically and persists for sometime following the DC event.

Applying the method to the model demonstrates that it is able to capture the large-scale responses to DC events, most notably for outgoing longwave radiation, but there are a number of important differences. For example, the DC signature of upper tropospheric humidity consistently covers a broader horizontal area than what is observed. In addition, the DC events move eastward in the model, but westward in the observations, and exhibit an unrealistic 24 h repeat cycle. Moreover, the modeled upper tropospheric cloud fraction anomalies – despite being of comparable magnitude and exhibiting similar longevity – are confined to a thinner layer that is closer to the tropopause and peak earlier than in observations. Finally, the modeled ice water content anomalies

ACPD

13, 13653–13684, 2013

Spatio-temporal impact of convection: methodology

M. S. Johnston et al.

Title Page

Abstract

Introduction

Conclusions

References

Tables

Figures

◀

▶

◀

▶

Back

Close

Full Screen / Esc

Printer-friendly Version

Interactive Discussion



at pressures greater than about 350 hPa are about twice as large as in the observations and do not persist as long after peak convection.

1 Introduction

The impact of tropical deep convective (DC) events on the upper troposphere and its overall effect on the climate remain important areas of uncertainty. Deep convection plays a vital role in the vertical transport of moisture and aerosols into the tropical upper troposphere, with a horizontal coverage that can span up to thousands of square kilometres. In addition to being a substantial source of precipitation, convection greatly influences the temperature lapse rate, humidity profile, and properties of clouds, having significant impacts on the top of atmosphere (TOA) radiation balance.

The impact of DC events on upper tropospheric water has been well studied, for example, by Mapes and Houze (1993); Webster et al. (1996); Chen et al. (1996); Chen and Houze (1997) (including references therein). Other studies have been more focused, studying the interaction of DC events on atmospheric variables with the incoming and outgoing radiation as well as the transport of moisture into to upper troposphere, for example, Eriksson et al. (2010); Tian et al. (2004); Soden (2004, 2000). Different techniques have been used to study aspects of DC events, for example, the diurnal cycle. Such techniques include a Lagrangian (Soden, 2004) and Eulerian (Zelinka and Hartmann, 2009) approaches.

Studies of DC events often rely on data acquired using geostationary sensors that are either infrared or optical. Optical sensors are daytime only and infrared radiation emission from the atmosphere and surface is severely absorbed by clouds (John et al., 2011; Liang et al., 2011). These limitations pose a problem when looking at in-cloud variables. On the other hand, the high temporal resolution of geostationary data allows for the tracking of the horizontal movement of humidity patterns and the cirrus anvil generated by DC events (Soden, 2004). Polar orbiting satellites, however, offer

Spatio-temporal impact of convection: methodology

M. S. Johnston et al.

Title Page

Abstract

Introduction

Conclusions

References

Tables

Figures

◀

▶

◀

▶

Back

Close

Full Screen / Esc

Printer-friendly Version

Interactive Discussion



a much wider range of observation sensors, including measurements at microwave wavelengths having a better cloud penetration capability.

A major drawback of observations from polar orbiting systems is the long time span between data acquisitions, a problem especially pronounced for low latitude regions (Kirk-Davidoff et al., 2005). Thus, they do not allow for the horizontal tracking of the time evolution of individual convective systems. However, mean responses of such systems can be derived, as shown by Zelinka and Hartmann (2009, hereinafter ZH09) and the anomalous response against an established background state can be ascertained. ZH09 approach is based on an objective identification of reference points centered in space and time on maxima in satellite-derived rain rates. Data from numerous satellite overpasses are then averaged, according to the distance in time and space to the identified DC event centre point, and a two or three-dimensional structure of different variables' response is obtained. An individual event will be sampled for only a few time bins and maybe for only part of the area considered, but when averaging over thousands of DC events, the mean patterns emerge. The data are averaged following the distance to fixed points, hence, this is an Eulerian approach.

The representation of the DC process and its impact on the atmosphere is an area of concern in climate projections from global climate models (GCM) (Randall et al., 2007). From a modelling perspective, problematic aspects are often that convection acts on sub-grid scales and interacts with low frequency Rossby and Kelvin waves (Bechtold et al., 2008). In most GCMs today, such processes are handled implicitly by various parametrisations that can generate considerable modelling uncertainties.

GCMs are constantly being evaluated as a means of addressing and reducing uncertainties. Such studies, with the aid of observations, tend to use straightforward seasonal or annual means, hence having an inherent time resolution of months or longer. But at such time scales, it is difficult to assess the realism and identify errors of individual processes (Stephens et al., 2010). Evaluations of GCMs on shorter time scales are not as prevalent because of the limited availability of suitable observational datasets. While there are some observations with a temporal resolution on the order of hours,

**Spatio-temporal
impact of convection:
methodology**

M. S. Johnston et al.

Title Page

Abstract

Introduction

Conclusions

References

Tables

Figures



Back

Close

Full Screen / Esc

Printer-friendly Version

Interactive Discussion



Spatio-temporal impact of convection: methodology

M. S. Johnston et al.

Title Page

Abstract

Introduction

Conclusions

References

Tables

Figures

◀

▶

◀

▶

Back

Close

Full Screen / Esc

Printer-friendly Version

Interactive Discussion



these are usually from ground-based stations (for example, the Atmospheric Radiation Measurement program, Qian et al., 2012), or from very short research campaigns, with limited regional and/or temporal coverage, e.g. Aerosol Radiation and Cloud Processes affecting Arctic Climate (ARCPAC) and Airborne Tropical Tropopause Experiment (ATTREX). The novel use of data from polar orbiting satellites introduced by ZH09 is extended in this study to diagnose convection-related and large-scale internal processes in climate models. The study is broken down into two parts. The first part re-examines the identification of the convective centre points, presents data compilations from sensors not considered by ZH09, and exemplifies the method for model evaluation by considering a single model (EC-Earth) and a single region (central Pacific). In Part II, the methodology is applied on a set of models, and for several regions, to give a broad evaluation of the realism with which tropical deep convection is simulated in climate models.

2 Data

2.1 Observations

2.1.1 Surface precipitation

Surface precipitation data, expressed as rain rate in mm h^{-1} , are taken from the TRMM Multi-satellite Precipitation Analysis (TMPA) 3B42 version 6/6A dataset. A description of the dataset is given by Huffman et al. (2007). Briefly, the dataset is a combination of multiple precipitation estimates from several satellite sources, both microwave and infrared, as well as both geostationary and polar orbiting. Whenever possible, surface rain gauges are used to scale the data. These data, when combined, provide a continuous TMPA hourly rain rate (RR) every 3 h. Each of these ordinal hour consists of data collected from ± 90 min of each hour. The dataset is provided on a 0.25° grid between $\pm 50^\circ$ latitude and with a time resolution of 3 h. For the purpose of this study, the TMPA

dataset is resampled to a 1° grid, which is slightly lower than EC-Earth's resolution (Sect. 2.2).

2.1.2 Upper tropospheric humidity

Upper tropospheric humidity (UTH), defined here as the Jacobian-weighted, average relative humidity with respect to ice ($\%RH_i$) from 500–200 hPa, is derived from the Advance Microwave Sounding Unit B (AMSU-B) and Microwave Humidity Sounder (MHS) sensors onboard operational satellites run by the National Oceanic and Atmospheric Administration (NOAA) and the European Organisation for the Exploitation of Meteorological Satellites (EUMETSAT). In this study, UTH retrievals are obtained from AMSU-B on NOAA-16 and NOAA-17, and from MHS on NOAA-18 and MetopA (all satellite observation angles included). The AMSU-B/MHS sensors have a swath of about 2300 km with a footprint resolution at nadir of approximately $20 \times 16 \text{ km}^2$ and around $64 \times 52 \text{ km}^2$ at its widest scan angles. UTH is retrieved using the brightness temperature (T_b) at 183.31(100) GHz, as described in Buehler and John (2005). This is channel 18 of AMSU-B and channel 3 of MHS.

An important aspect of this dataset is cloud penetrability. The UTH retrieval assumes no scattering but this normally sound assumption begins to break down in DC clouds. Ice particles scatter emitted microwave radiation and lower the T_b thereby causing an overestimation of UTH. Although these measurements are much less sensitive to clouds than those from IR sensors (John et al., 2011), scattering is of particular significance in convective regions, and the degree of scattering is also dependent on satellite viewing angle. This is taken into account when screening the data, which involves the use of a cloud filter described in Buehler et al. (2007). The two-part filter uses a scan angle-dependent T_b threshold, along with a filter considering the T_b difference to the neighbouring channels (19 or 20 for AMSU, and 4 or 5 for MHS).

Since data from several satellites are used, inter-satellite T_b biases become an issue. Such biases have been investigated by John et al. (2013) and found not to be signifi-

Spatio-temporal impact of convection: methodology

M. S. Johnston et al.

Title Page

Abstract

Introduction

Conclusions

References

Tables

Figures

◀

▶

◀

▶

Back

Close

Full Screen / Esc

Printer-friendly Version

Interactive Discussion



cantly large that they prevent the combination used in this study. For the remainder of this study, this UTH dataset will simply be referred to as AMSU.

2.1.3 Cloud fraction and cloud ice water content

The nadir-looking CloudSat cloud-profiling radar operates at 94 GHz with a horizontal resolution of ~ 2 km and a vertical resolution of 500 m. Since June 2006, the instrument has provided height resolved cloud properties, for example, ice water content and cloud fraction (Stephens et al., 2002). CALIOP is a space-borne lidar, on-board the CALIPSO satellite, that operates at wavelengths 532 nm and 1064 nm (Winker et al., 2007). This study uses the recently developed CloudSat and CALIPSO Ice Cloud Property Product (2C-ICE) which combines data from collocated CloudSat 2B-GEOPROF data and the measured attenuated backscattered coefficients from CALIPSO's 532 nm channel. A detailed technical description of the 2C-ICE dataset can be found on the CloudSat website: <http://www.cloudsat.cira.colostate.edu/data/CDlist.php?go=list&path=/2C-ICE>.

The scattering properties at microwave and visible wavelengths lead to very different sensitivities of CloudSat and CALIPSO. Thin clouds consisting of smaller particles are only detected by CALIPSO, while parts of the atmosphere with a thicker cloud layer above are only probed by CloudSat. The vertical extension of the overlapping region between the two instruments differs depending on several cloud variables, such as liquid and ice water mass and the associated particle size distributions. For the tropical region, the point where CloudSat and CALIPSO show the same average cloud frequency is found consistently close to 200 hPa, and for lower (higher) altitudes the CloudSat frequency is, in rough terms, a factor two higher (lower) than CALIPSO (see Johnston et al., 2012, Fig. 4).

Spatio-temporal impact of convection: methodology

M. S. Johnston et al.

Title Page

Abstract

Introduction

Conclusions

References

Tables

Figures



Back

Close

Full Screen / Esc

Printer-friendly Version

Interactive Discussion



2.1.4 Radiation

TOA outgoing longwave radiation (OLR) flux observations are provided by the Cloud and Earth Radiant Energy System (CERES) sensors onboard the Aqua and Terra satellites. The hourly Single Satellite Footprint (SSF) cloud edition 3A hourly dataset is chosen for this study. This product combines CERES sensor data with information from the Moderate Resolution Imaging Spectroradiometer (MODIS) and the Visible and Infrared Scanner (VIRS) sensors. The level 2 SSF dataset is taken from both satellites. Because each sensor has been radiometrically inter-calibrated, the two sensors can be considered as one. The data are then gridded to a regular grid ($\approx 0.7^\circ$) following the resolution of EC-Earth (Sect. 2.2). An in-depth description of the CERES sensor is given by Wielicki et al. (1996) and a discussion of the measurement uncertainty, which is primarily due to calibration error and estimated to be about $\pm 5 \text{ W m}^{-2}$, can be found in Loeb et al. (2009). Level 2 data do not contain albedo and therefore is calculated using a formulation obtained from the CERES team.

2.2 Climate model

The global climate model used in this study is an emerging version of EC-Earth, version 3 (uncoupled). This version is based on the seasonal forecast version of the European Centre for Medium-Range Forecast (ECMWF) Integrated Forecast System (IFS) Cycle 36r4 (<http://www.ecmwf.int/research/ifsdocs>). The basic configuration used has a horizontal resolution set to $\approx 0.7^\circ$ and vertically there are 91 staggered, vertical hybrid levels extending to roughly 85 km. The model time step is set to 45 min and the output frequency is every 3 h. Prescribed boundary conditions, such as sea surface temperature, are taken from ERA-Interim monthly means.

In this study a subset of variables are compared within a model-to-retrieval framework. They are RR, UTH, cloud fraction, cloud ice water content, OLR, and albedo. The radiation and precipitation variables are accumulated fields over the output frequency

ACPD

13, 13653–13684, 2013

Spatio-temporal impact of convection: methodology

M. S. Johnston et al.

Title Page

Abstract

Introduction

Conclusions

References

Tables

Figures

◀

▶

◀

▶

Back

Close

Full Screen / Esc

Printer-friendly Version

Interactive Discussion



time, and are converted to mean values and rates, respectively, by division with the output frequency. Non-accumulated variables are interpolated to the centre.

The surface precipitation used in this study is the sum of stratiform and convective precipitation. UTH is taken as the grid-box mean relative humidity, with respect to ice.

For ice water content, precipitating ice from convective core is added to the model's stratiform cloud ice and precipitating snow water contents in order to better match what is measured by 2C-ICE sensors. The convection parametrization produces convective precipitation from the convective updraught core and also detrains cloud water/ice into to the large-scale (stratiform) cloud scheme. Stratiform cloud ice and precipitating snow are therefore associated with each convective event and are both represented as prognostic variables in the model. Moreover, while both stratiform cloud ice and precipitating snow are both considered in the radiation calculation, the convective core ice is not. Albedo, α , is calculated as

$$\alpha = 1 - \frac{SW_{\text{net}}}{SW_{\text{in}}}, \quad (1)$$

where SW_{net} is the model's TOA net (incoming minus reflected) short wave radiation, and SW_{in} is the product of the solar constant and the cosine of the solar zenith angle. Albedo was derived for zenith angles between 0–85°. Inclusion of higher angles was found to give less stable results.

3 Method

In this study, the core idea of ZH09 is maintained, but the methodology is elaborated in some aspects. The motivation for some changes arises from the fact that the selection of DC events in ZH09 ignored the potential for cross-contamination of the time bins, which may have caused an unintentional smoothing of the results, and that their definition of the background state included the anomaly itself. Following a recommendation

Spatio-temporal impact of convection: methodology

M. S. Johnston et al.

Title Page

Abstract

Introduction

Conclusions

References

Tables

Figures

◀

▶

◀

▶

Back

Close

Full Screen / Esc

Printer-friendly Version

Interactive Discussion



in ZH09, the spatio-temporal window is increased. This section summarises the ZH09 method and the adjustments made in this study.

3.1 Zelinka and Hartmann (2009)

ZH09 used data from polar orbiting satellites to assess atmospheric effects of DC events during the period 2003–2005 for a part of the equatorial Pacific Ocean (5–15° N and 120–160° E). Identification of DC events was done through RR from the TMPA dataset (same version as used here). This multiple-satellite dataset allows for the identification of DC events with a spatial and temporal resolution of 0.25° and 3 h, respectively, though ZH09 analysed TMPA after first averaging the data to 1° resolution.

Candidates for DC events were selected from a RRs exceeding the 90th percentile ($> 1.6 \text{ mm h}^{-1}$), which contributed about 57 % of the total $\text{RR} > 0$ for that region and period 2003–2005. Adjacent grid spaces containing RRs exceeding the threshold were averaged into one distinct realisation. This method assumes that the selected RR values, now taken as the centre point in both space and time for peak convection, coincides closely with the strongest convection.

A typical DC event can cover thousands of km^2 , and the resulting effects on the atmosphere extend over even larger areas. Accordingly, ZH09 considered a geographical area of size $11^\circ \times 11^\circ$ around each DC event's centre point over a time range of $\pm 24 \text{ h}$ divided into 3 h time bins. They calculated the mean of all data from satellite passes falling into each spatio-temporal bin over the 3 yr period, resulting in a composite depicting the mean evolution of the DC events observed. This averaging compensates for the fact that a specific DC event is observed by a sun-synchronous sensor, at best, twice every 24 h separated by 12 h. Figure 1 exemplifies the outcome of this averaging process.

Spatio-temporal impact of convection: methodology

M. S. Johnston et al.

Title Page

Abstract

Introduction

Conclusions

References

Tables

Figures

◀

▶

◀

▶

Back

Close

Full Screen / Esc

Printer-friendly Version

Interactive Discussion



3.2 Modifications of the methodology

The selected geographical area for the study is bounded by $\pm 15^\circ$ in latitude and 140° to 260° E in longitude. A sub-area around New Guinea is masked out in order to avoid land-based convection that has a different diurnal cycle. The region described is used for selecting centre points of DC event, but the data that are compiled can extend outside the given boundaries. The time period used is 2007–2008. The relative time window is set to ± 48 h, and the spatial window is set to $21^\circ \times 21^\circ$.

There are cases when two or more RR values above the threshold occur in adjacent space or time bins and are highly likely part of the same convective system. Selecting such DC cases would result in overlap in the time dimension and introduce a smoothing effect. This is solved by sorting the DC events in order of decreasing RR. The position of the highest RR is classified as a DC centre, and all equal or lesser RRs within $12^\circ \times 12^\circ$ and ± 18 h are removed from the processing chain. The highest remaining RR becomes a new DC centre and so forth.

Using satellite RR retrievals, a centre point for each of the most intense DC events inside the region is determined, in both time, t_0 and space, (x_0, y_0) . This is followed by a processing of data from a range of satellite sensors. Each satellite observation, at (x_s, y_s, t_s) , contributes to the final average for the relative time (Δt), latitude (Δy) and longitude (Δx) bin encompassing $(\Delta x, \Delta y, \Delta t) = (x_s - x_0, y_s - y_0, t_s - t_0)$. That is, the satellite data are averaged according to the time and geographic distance to the DC events centre points. The temporal bins are 3 h wide, with -48 h and 48 h as first and last centre points. With the exception of the TMPA dataset, which is resampled to 1° , the latitude and longitude bins are $\approx 0.7^\circ$ wide and have a total coverage of $\approx 21^\circ$ in each dimension. For satellite retrievals that provide profile information, the averaging also involves vertical bins.

Title Page

Abstract

Introduction

Conclusions

References

Tables

Figures



Back

Close

Full Screen / Esc

Printer-friendly Version

Interactive Discussion



3.3 Expanding the study

A largely different set of sensors are considered in this study that both complements the results already reported in ZH09 and also simplifies the comparison with models. Cloud interference is not only an inherent issue for satellite sounding but also complicates strongly the comparison to model data. For this reason, “all sky” OLR has been chosen instead of the “clear sky” OLR. Also, an additional extension to this study is the examination of the DC event’s effect on the TOA net short wave radiation through its effect on albedo. In addition, UTH is taken from microwave observations rather than from AIRS. This is motivated by the need to reduce cloud interference in the data because the AIRS retrieval rejects scenes with a cloud fraction $> 70\%$ (John et al., 2011; Liang et al., 2011). Rather than using passive cloud retrievals, as in ZH09, this study employs the active sensors onboard CloudSat and CALIPSO to derive cloud fraction and cloud ice water content.

The modified ZH09 approach is applied to evaluate deep convection in a GCM. DC events inside the model are identified using RR. Verification of deep convection is done with the use of a diagnostic flag that signifies when the deep convection parametrization scheme is active. The model and TMPA are processed in their native grids using different thresholds for the DC event’s RR because of the difference their peak RR intensities. The maximum RR in the model is $\approx 10 \text{ mm h}^{-1}$, while in the TMPA dataset it is $\approx 70 \text{ mm h}^{-1}$. Taking the 90th percentile of each source results in a much larger TMPA sample size than for the model. The TMPA sample would in this case introduce a bias towards the weaker cases. This is solved by taking the strongest 11 000 cases in each dataset. Matching the sample size removes the need to consider the different RR intensities and removes sampling biases.

Spatio-temporal impact of convection: methodology

M. S. Johnston et al.

Title Page

Abstract

Introduction

Conclusions

References

Tables

Figures

◀

▶

◀

▶

Back

Close

Full Screen / Esc

Printer-friendly Version

Interactive Discussion



4 Results and discussion

In comparison to earlier works (ZH09 and Horváth and Soden, 2008; Soden, 2004), this study takes a step forward by extending both the temporal and horizontal coverage. Perhaps the most important aspect is the extension backward in time to obtain a more robust estimate of the background state. On the other hand, there exist studies following the detrained air over 5 days using trajectories estimated by wind data taken from models (Wright et al., 2009; Luo and Rossow, 2004), but those analysis are restricted to the period after peak convection.

4.1 Rain rate statistics

The 24 h distribution of TMPA precipitation is relatively flat (lower left figure), especially for light precipitation. However, a discernible pattern emerges in the 24 h distribution of DC events (lower right figure), where there are four modes. Two modes are associated with RRs below $\sim 20 \text{ mm h}^{-1}$ and are most frequently observed around 01:00 and 14:00 LST. Above $\sim 30 \text{ mm h}^{-1}$, another two modes, with observed times around 05:00 and 19:00 LST, can be seen. Similar findings were reported by Mapes and Houze (1993), who found a shift in the peak times of DC events based on their horizontal coverage (intensity). Alcala and Dessler (2002, Fig. 6) also found some variation on the peak times for DC events over ocean, albeit for one season. These results compare somewhat differently with those Nesbitt and Zipser (2003) who looked at the diurnal cycle of rainfall and convective intensity from the Tropical Rainfall Measuring Mission over a three-year period for tropical ocean and land areas. They confirm the peak in DC events in the early morning over ocean areas but not the late afternoon to early evening peak. An examination of the model's DC events (not shown) reveals that the two modes seen in the most intense events are missing.

One of the most important points underscored by Fig. 2 is the large differences between RR from the model and observation. Resampling the TMPA data to roughly one and three times the model resolution failed to show convergence. The differences

Title Page

Abstract

Introduction

Conclusions

References

Tables

Figures



Back

Close

Full Screen / Esc

Printer-friendly Version

Interactive Discussion



here are well beyond any reasonable uncertainty in the TMPA dataset. Similar findings, highlighting the poor representation of surface precipitation in models, were reported by Stephens et al. (2010).

4.2 Averaging considerations

5 With the exception of the TMPA dataset, all satellites used in the study are in sun-synchronous orbits. A sensor in an orbit of this type performs measurements around the Equator at two fixed local solar times, 12 h apart. This has the consequence that the placement in space and time of peak convection becomes significant because the peaks occur at different times and seem to be different for the weakest and strongest cases. This means that some time bins will be preferentially influenced by the strongest DC events. Thus, an aliasing effect is created between the sampling of the sun-synchronous satellites and the diurnal cycle of convection. The overpass times of the sun-synchronous satellites have a 12 h repetition pattern that is, therefore, reflected in the results. This aliasing is apparent in Fig. 1, where averages from two different sensors are compared. For CERES Aqua, discontinuities in the time series are seen at -12 h, 0 h, and 12 h, while for CERES Terra this pattern is shifted to -15 h, -3 h, and 9 h, consistent with the fact that Terra has a 3 h earlier ascending node.

Aliasing effects are much less pronounced in the results of ZH09, despite the fact that they only used datasets from a single sun-synchronous satellite (TMPA excluded). As can be seen in Fig. 3, at the geographical centre point, a high RR is maintained between at least -3 h and 3 h. In ZH09 the RR data were analysed for each time bin in isolation (Sect. 3), and it is likely that many persistent intense convective systems were each inserted as separate DC events, causing the same DC event to be sampled multiple times. The area selected by ZH09 includes land-based convection with another diurnal cycle, which can also affect the results.

Spatio-temporal impact of convection: methodology

M. S. Johnston et al.

Title Page

Abstract

Introduction

Conclusions

References

Tables

Figures

◀

▶

◀

▶

Back

Close

Full Screen / Esc

Printer-friendly Version

Interactive Discussion



4.3 Spatial patterns

The spatio-temporal evolution of RR (TMPA resampled to 1°), UTH, cloud ice water content, cloud fraction, albedo, and OLR are shown in Figs. 3 and 4. Figure 4 shows the anomalies isolated from the background state for a subset of the variables that are least affected by aliasing. The background state is taken as the zonal mean over the first 12 h of the composite period. More precisely, for each latitude, the mean state is computed as the mean over all longitude bins of the -48 h to -39 h time bins. Because ZH09 computed the background state as the mean over all horizontal bins for the entire composite period, it included the anomaly and was therefore perturbed from a true background state. One must bear in mind that the horizontal extent of the anomaly is the mean of the 11 000 cases and does not represent a single DC event. In this section, the words “mean” and “anomaly” will refer to Figs. 3 and 4 respectively.

4.3.1 Observations

High RR means are strongly focused around the DC centre points and significant deviations from the background state are confined to ± 6 h, $\pm 2^\circ$ in latitude, and $\pm 3^\circ$ in longitude. The region of elevated mean RRs propagates westward at $\approx 4 \text{ m s}^{-1}$. This region of higher RR is better illustrated in the anomaly plot (Fig. 4) where a somewhat symmetrical pattern of change in RR is evident and centered around the time of peak convection. ZH09 also identified a mean westward movement of about $\approx 6 \text{ m s}^{-1}$, consistent with the movement of synoptic disturbances observed in the ITCZ (Reed and Recker, 1971).

The AMSU data shows an area of increased mean UTH about 0 h. The horizontal extent of this area then continues to increase radially after peak convection until about 6 h. However, the anomaly continues to expand up to 18 h. The true extent of the anomaly and its magnitude remain undetermined because the moisture expands outside the box sometime between 15 h and 18 h. Both the mean and anomaly plots show elevated levels of UTH persisting long after peak convection.

Spatio-temporal impact of convection: methodology

M. S. Johnston et al.

Title Page

Abstract

Introduction

Conclusions

References

Tables

Figures

◀

▶

◀

▶

Back

Close

Full Screen / Esc

Printer-friendly Version

Interactive Discussion



Spatio-temporal impact of convection: methodology

M. S. Johnston et al.

Title Page

Abstract

Introduction

Conclusions

References

Tables

Figures

◀

▶

◀

▶

Back

Close

Full Screen / Esc

Printer-friendly Version

Interactive Discussion



The cloud ice water content and cloud fraction results are “noisy”. Although Cloud-Sat and CALIPSO provide a high number of observations, the atmospheric volume sampled is roughly three orders of magnitude smaller than for passive instruments. This due largely to the sensor’s respective swaths which are ~ 2 km for CloudSat and 2300 km for AMSU-B. This gives a much smaller sampling coverage for narrow-swath instruments. In addition, the time series are also disturbed by aliasing. The cloud fraction and cloud ice content are lower at -12 h, 0 h, and 12 h than for the adjacent time bins (not shown). Because of these reasons cloud ice content and cloud fraction variables are not included in Fig. 4. While these variables are problematic, they still offer an opportunity to get some idea of the 3-D response which will be taken up in Sect. 4.4.1.

A peak in the albedo (≈ 0.43) occurs sometime around 3 h. While the UTH and OLR anomalies grow in spatial extent after peak convection, this is not reflected in the albedo and suggests a reduction in the cloud optical thickness radially from the center of the core, but with a stronger gradient latitudinally. The drop in mean OLR due to deep convection culminates around 3 h at $\approx 80 \text{ W m}^{-2}$, and there is a distinct broadening of the spatial extent of the OLR anomaly after peak convection that is highly correlated both with the horizontal extent and persistence of the UTH anomaly.

All variables are centered on the time of peak convection that is established by the RR. It is likely the reason why the mean and anomaly RR display a symmetrical pattern around 0 h. However, the other variables, with the exception of the 2C-ICE dataset that has unstable results out to ± 18 h, display a distinct asymmetrical pattern where the effect of a DC event persists for a long time after peak convection. In the case of the UTH and OLR, the effects persists beyond 18 h.

4.3.2 EC-Earth

The following section uses the ZH09 method to evaluate DC processes in a CGM. The discussion about the model’s performance is left open in this study because a deeper analysis into some of the findings is required. This is reserved for part II of the study where comparison to some other prominent models will give better perspectives.

Spatio-temporal impact of convection: methodology

M. S. Johnston et al.

[Title Page](#)[Abstract](#)[Introduction](#)[Conclusions](#)[References](#)[Tables](#)[Figures](#)[⏪](#)[⏩](#)[◀](#)[▶](#)[Back](#)[Close](#)[Full Screen / Esc](#)[Printer-friendly Version](#)[Interactive Discussion](#)

The compilation of model data is relatively straightforward, as the model data are continuous in all dimensions, with the exception of albedo. Consequently, no aliasing effect is seen in the other variables. The RR shows a similar symmetry about the 0 h to the observations but indicates a mean eastward movement of DC events.

5 This implies a predominance of the Kelvin waves over easterly waves, in contrast to the observations (Lin et al., 2008). The model UTH shows a higher background mean than the observation and the corresponding anomaly is very extensive covering 12° longitude \times 4° latitude, significantly larger than the response seen in AMSU mean results. However, model UTH anomaly ceases to expand in horizontal extent after 6 h, in contrast to the the observation.

10 The cloud ice content and cloud fraction follow the ITCZ pattern at 200 hPa. There is a rather high background cloud ice content of $\sim 20\text{--}70\text{ mg m}^{-3}$. At its maximum, the mean cloud ice content can exceed 200 mg m^{-3} . This occurs sometime around 3 h with an horizontal coverage of about $4^\circ \times 4^\circ$. The model shows significant decrease of ice by 9 h. Also, the mean 200 hPa cloud fraction exceeds its background of $\sim 40\%$ from 0–18 h, and the peak in the mean DC events occurs around 6 h.

Several factors complicate the interpretation of the albedo response in the model. The derivation of albedo is limited to daytime and is greatly affected by the solar zenith angle and the representation of DC diurnal cycle in the model. There are four modes in the observational DC diurnal cycle (Fig. 2 lower right) but only two are found in EC-Earth (not shown). The model misses the mode of the two most intense DC events that occur mid morning and in the evening. This results in a limitation of the probability that all time bins will occur during daylight hours and at low solar zenith angles. This creates especially strong dependence on the accuracy of the model's diurnal cycle representation. The EC-Earth model configuration chosen is close to that submitted to the fifth Coupled Model Intercomparison Project. In this configuration the radiation scheme is called every 3 h, rather than 45 min (the model time step), and on a coarser horizontal grid; thus, the diurnal cycle generated will be based on fewer temporal and horizontal grid points and interpolated in-between. This treatment of the radiation is

5
10
15
20
25

Spatio-temporal impact of convection: methodology

M. S. Johnston et al.

Title Page

Abstract

Introduction

Conclusions

References

Tables

Figures

⏪

⏩

◀

▶

Back

Close

Full Screen / Esc

Printer-friendly Version

Interactive Discussion



a computational trade-off that could contribute to the differences with respect to CERES (Fig. 3). One way to separate the effects of the model's representation of the diurnal cycle of DC events and the radiative effects of DC events is to restrict the solar zenith angle. This limitation produces much more stable results that matches more closely the CERES observation. Therefore, what is seen in Figs. 3 and 4 are model albedo restricted to cases where the solar zenith angles are $\leq 45^\circ$.

While the many oscillatory effects have been removed by the solar angle restriction, the model albedo still misses much of the the extent and timing of the elevated reflection caused by the deep convective clouds. A maximum of ~ 0.3 somewhere between 3–6 h is significantly less than what is seen in CERES. Also, some time bins, –9 h and 6 h, for example, still show a slightly higher albedo that is broader, latitudinally, than seen in the observation, which suggests that the optical depth of clouds away from the DC events is too high.

A maximum decrease in OLR occurs sometime from 3–6 h. At the DC center between 0 h and 3 h, the model is clearly showing a higher mean OLR by about $\sim 10 \text{ W m}^{-2}$. The dissipation in the model occurs a bit more slowly, by about 3 h, than seen in the observation. The model OLR anomaly does not follow a spreading-out pattern that is more in line with the UTH. Surprisingly, the OLR anomaly begins to shrink after 9 h even though the UTH continues to spread out. This is not in agreement with CERES and AMSU.

4.4 Spatially averaged anomaly timeseries

The time-evolution of geographically averaged anomalies is shown in Figs. 5 and 6. The domain size for this additional averaging is set to 13° latitude and 21° longitude in order to avoid including areas outside the impact region of the convection. The evolution of domain average albedo, OLR, UTH, and RR anomalies over 96 h is shown in Fig. 5, while vertical profiles of spatial-mean cloud ice content and cloud fraction are shown in Fig. 6.

Spatio-temporal impact of convection: methodology

M. S. Johnston et al.

Title Page

Abstract

Introduction

Conclusions

References

Tables

Figures

◀

▶

◀

▶

Back

Close

Full Screen / Esc

Printer-friendly Version

Interactive Discussion



Rather than exhibiting relatively smooth and monotonic growth and decay, the spatial average anomalies, with the exception of the TMPA RR, tend to be rather oscillatory in both the observation and model, with several local minima and maxima notable in the UTH, OLR, and albedo curves. These features, which in many cases are likely sampling artefacts, complicate attempts to objectively quantify the anomaly's magnitude, onset, and duration. What is discussed in the following sections Sect. 4.4.1 and Sect. 4.4.2 are more subjective interpretations of Figs. 5 and 6.

4.4.1 Observations

At its most intense, the mean RR anomaly rises 0.04 mm h^{-1} above the background state. There is a monotonic increase of the RR starting from about -15 h to peak convection and decreasing in a similar manner up to 27 h , making the positive anomaly more persistent. As the RR dataset is resampled to a 1° grid, there is no clearly defined peak at 0 h . The OLR and UTH anomalies are in close agreement with each other showing a high degree of correlation. However, the UTH seems to peak a bit later than the OLR. UTH anomaly appears to reach a maximum at $\sim 18 \text{ h}$, about 3 percentage points above the background state. Similarly to the OLR, the UTH anomaly lasts for longer time after peak convection. The OLR anomaly peaks at about 3 h at about -8 W m^{-2} . Full relaxation is not achieved during the 48 h period after peak convection. Finding a maximum albedo is hampered by these artefacts, however, the results are well correlated with the OLR.

The maximum of the cloud fraction occurs about 10 h after peak convection, but, for ice water content, this occurs sometime around peak convection. Figure 6 shows the temporal evolution of the spatially-averaged and smoothed profiles of cloud fraction (left column) and cloud ice content (right column) between 500 and 100 hPa . Cloud fraction response is greatest ($\sim 4 \%$) at pressures $\leq 300 \text{ hPa}$, but there is also a clear response at pressures $\geq 300 \text{ hPa}$ reflecting the core of the convective event. In contrast, the largest cloud ice content anomalies ($\sim 10 \text{ mg m}^{-3}$) occur at pressures $\geq 300 \text{ hPa}$. The maximum cloud fraction occurs between 0 h and 20 h , while for the ice water content,

this occurs around 0 h, but the moving-average makes it difficult to say whether the anomaly is asymmetric about 0 h.

4.4.2 EC-Earth

The model OLR follows closely the observation and has, roughly, a similar timing of its minimum after peak convection (Fig. 5) as seen in the observation. However, the model's response is about $\sim 3 \text{ W m}^{-2}$ too high 10–20 h after peak convection. With regards to albedo, the restriction placed on the solar zenith angle, while producing a better mean composite match with CERES, results in a reduced sample size. Nevertheless, the model albedo follows the observation closely.

Using the TMPA resampled to a 1° resolution, which is slightly higher than the model resolution, the maximum value of the time series agrees with the observations, peaking around the 0 h. There is a flattening of the observations due to the resampling of the data. The model's RR anomaly has a higher peak value and is more oscillatory than the TMPA observation. In the case when the TMPA dataset is interpolated to match the model (not shown), the peak TMPA RR becomes significantly higher than the model, but this method involves some amount of interpolation. There are two secondary peaks at -24 h and 24 h, indicating that the model has a diurnal repetition pattern for convection. The anomaly culminates at about 0.06 mm h^{-1} but, contrary to the observation, the persistence of the anomaly is greater prior to convection than after.

Figure 6 clearly illustrates the cloud fraction anomaly is greatest at pressures ≤ 300 hPa, reaching a maximum of between 0 h and 3 h. While the response of clouds in the upper troposphere is in good agreement with the observation, there is a clear underestimation of clouds at pressures greater than 300 hPa in the model. The signature of the DC event anomaly extends farther into the upper troposphere and injects a greater quantity of ice at higher pressure levels than seen in the 2C-ICEs smoothed results. Ice reaching levels 200–150 hPa persists for nearly 36 h and is present even when other convective activity is initiated later on. The timing of cloud ice maximum is situated around 0 h, but in the observation, the maximum is somewhat later. The dif-

Spatio-temporal impact of convection: methodology

M. S. Johnston et al.

Title Page

Abstract

Introduction

Conclusions

References

Tables

Figures



Back

Close

Full Screen / Esc

Printer-friendly Version

Interactive Discussion



Spatio-temporal impact of convection: methodology

M. S. Johnston et al.

Title Page

Abstract

Introduction

Conclusions

References

Tables

Figures

⏪

⏩

◀

▶

Back

Close

Full Screen / Esc

Printer-friendly Version

Interactive Discussion



ference in the production of ice in the model's DC scheme is clear when compared to the other minor convective events captured at ± 24 h. The diagnostic treatment, or the falling out of convective precipitating ice, between time steps, is clearly evident in the rapid removal of the higher ice water content values right after peak convection. This is in contrast to the ice injected near 150 hPa. Part of the reason for this is the conversion of the convective ice flux to ice densities which is added to the model output offline and is calculated using an assumed constant fall speed for the precipitating ice. From Fig. 6 lower right plot, it is clear that convection in the model operates on a 24 h cycle, and the duration of the diagnostic convective ice flux, present only when the deep convection parametrization is active, is limited.

5 Summary and conclusion

Evaluation and continued development of climate models requires novel approaches for confronting GCM output with observations, especially at the process level. In this study, one such methodology is elaborated and initial results are reported. Tropical deep convection is the main focus, but the method should be applicable on all convection of localised nature.

The ZH09 study has been improved by expanding the filtering of DC events to the time dimension, which reduces multiple sampling of a single event but unfortunately exposes the method's vulnerability to aliasing effects, especially when relying on single sun-synchronous satellites such as CloudSat. This problem can be addressed by using datasets consisting of data from multiple satellites, such the AMSU dataset. Unlike in ZH09, the background state is computed from the first 12 h time bins starting 48 h prior to peak convection. Observed DC events move westward at about 4 ms^{-1} , on average. Humidification of the upper troposphere ($\%RH_i$) from DC events results in a roughly 2 % increase at maximum, and can persist longer after peak convection than the 48 h relative time window used in this study. High values of UTH and OLR are seen over a large horizontal area that broadens after peak convection. The albedo anomaly

**Spatio-temporal
impact of convection:
methodology**

M. S. Johnston et al.

Title Page

Abstract

Introduction

Conclusions

References

Tables

Figures

◀

▶

◀

▶

Back

Close

Full Screen / Esc

Printer-friendly Version

Interactive Discussion

shows significantly narrower horizontal extent than both the OLR and UTH. Maximum cloud fraction anomaly ($\sim 4\%$) is reached between 250 and 200 hPa and persists for over 50 h. For cloud ice water content, a maximum of about $\sim 8 \text{ mg m}^{-3}$ is concentrated around 0 h and at levels close to 450 hPa, and is confined to pressure levels > 200 hPa.

The diagnosis of convection in EC-Earth shows that, despite some differences, the model is able to capture the essential signatures of DC events in good agreement with the observations. The upper tropospheric humidity anomaly ($\%RH_i$) peaks about the same time as the AMSU dataset and indicates a similar $\sim 2\%$ maximum. The mean and anomalous OLR agree with the observation, but an overestimation of the mean OLR by $\sim 3 \text{ W m}^{-2}$ can be seen in the DC core. The albedo anomaly follows the general pattern of the observation but its magnitude is significantly underestimated. Convection in the model lasts about 24 h and is then repeated either as shallow or mid-level convection. The model is found to under-represent clouds fraction at pressure levels > 350 hPa. Nam et al. (2012), using a cloud simulator, also found similar results for cloud fraction in other GCMs. The vertical profile of the cloud fraction anomaly indicates that most of clouds generated by DC events are concentrated at pressures ≤ 300 hPa and persist longer than 48 h after peak convection. Cloud ice water content anomalies are much larger than in the observation due to the diagnostic convective ice flux from the convective parametrization and tend to be confined to lower altitudes where the cloud fraction anomalies are small.

The extension of the ZH09 methodology to a climate model enables one to deduce the mean atmospheric response to convection. For example, the mean horizontal extent of anomalies and their magnitude can be ascertained, with directly comparable satellite estimates. However, direct objective properties about the model anomalies is hampered by oscillatory patterns in the timeseries of many of the variables. Therefore, we leave this task to future studies where these artefacts can be thoroughly investigated and properly addressed. Furthermore, the purpose of this study is to show the applicability of the method on a climate model. Robust conclusions about the model is

therefore left for a more detailed and rigorous study which will be carried out in part II of the study.

Acknowledgements. The authors would like to thank Jean-Jacques Morcrette and Peter Bechtold from the European Centre for Medium-Range Weather Forecasts (ECMWF), Martin Evaldsson (Swedish Meteorological and Hydrological Institute (SMHI), Andreas Skyman, and Ole-Martin Christensen for their technical and scientific help with this study. The authors would also like to thank Stefan Buehler at Luleå University of Technology for his input on the UTH retrievals and satellite sampling. The TMPA data were provided by the NASA/Goddard Space Flight Center's Mesoscale Atmospheric Processes Laboratory and PPS, which develop and compute the TMPA as a contribution to TRMM. In addition the CERES data were obtained from the NASA Langley Research Center Atmospheric Science Data Center. Also we would like to acknowledge the NASA CloudSat project who provided the CloudSat-CALIPSO dataset used in this project. The contribution of Mark D. Zelinka was performed under the auspices of the US Department of Energy by Lawrence Livermore National Laboratory (LLNL) under Contract DE-AC52-07NA27344 and was supported by the LLNL Institutional Postdoctoral Program. Salomon Eliasson was supported by the Swedish National Space Board.

References

- Alcala, C. M. and Dessler, A. E.: Observations of deep convection in the tropics using the Tropical Rainfall Measuring Mission (TRMM) precipitation radar, *J. Geophys. Res.*, 107, 4792, doi:10.1029/2002JD002457, 2002. 13665
- Bechtold, P., Köhler, M., Jung, T., Doblas-Reyes, F., Leutbecher, M., Rodwell, M. J., Vitart, F., and Balsamo, G.: Advances in simulating atmospheric variability with the ECMWF model: from synoptic to decadal time-scales, *Q. J. Roy. Meteor. Soc.*, 134, 1337–1351, doi:10.1002/qj.289, 2008. 13656
- Buehler, S. A. and John, V. O.: A simple method to relate microwave radiances to upper tropospheric humidity, *J. Geophys. Res.*, 110, D02110, doi:10.1029/2004JD005111, 2005. 13658
- Buehler, S. A., Kuvatov, M., Sreerexha, T. R., John, V. O., Rydberg, B., Eriksson, P., and Notholt, J.: A cloud filtering method for microwave upper tropospheric humidity measurements, *Atmos. Chem. Phys.*, 7, 5531–5542, doi:10.5194/acp-7-5531-2007, 2007. 13658

Spatio-temporal impact of convection: methodology

M. S. Johnston et al.

Title Page

Abstract

Introduction

Conclusions

References

Tables

Figures

◀

▶

◀

▶

Back

Close

Full Screen / Esc

Printer-friendly Version

Interactive Discussion



Spatio-temporal impact of convection: methodology

M. S. Johnston et al.

Title Page

Abstract

Introduction

Conclusions

References

Tables

Figures

◀

▶

◀

▶

Back

Close

Full Screen / Esc

Printer-friendly Version

Interactive Discussion



Chen, S. S. and Houze, R. A.: Diurnal variation and life-cycle of deep convective systems over the tropical Pacific warm pool, *Q. J. Roy. Meteor. Soc.*, 123, 357–388, doi:10.1002/qj.49712353806, 1997. 13655

Chen, S., Houze, R., and Mapes, B.: Multiscale variability of deep convection in relation to large-scale circulation in TOGA COARE, *J. Atmos. Sci.*, 53, 1380–1409, 1996. 13655

Eriksson, P., Rydberg, B., Johnston, M., Murtagh, D. P., Struthers, H., Ferrachat, S., and Lohmann, U.: Diurnal variations of humidity and ice water content in the tropical upper troposphere, *Atmos. Chem. Phys.*, 10, 11519–11533, doi:10.5194/acp-10-11519-2010, 2010. 13655

Horváth, Á. and Soden, B. J.: Lagrangian diagnostics of tropical deep convection and its effect upon upper-tropospheric humidity, *J. Climate*, 21, 1013–1028, doi:10.1175/2007JCLI1786.1, 2008. 13665

Huffman, G. J., Bolvin, D. T., Nelkin, E. J., Wolff, D. B., Adler, R. F., Gu, G., Hong, Y., Bowman, K. P., and Stocker, E. F.: The TRMM Multisatellite Precipitation Analysis (TMPA): quasi-global, multiyear, combined-sensor precipitation estimates at fine scales, *J. Hydrometeorol.*, 8, 38–55, doi:10.1175/JHM560.1, 2007. 13657

John, V. O., Holl, G., Allan, R. P., Buehler, S. A., Parker, D. E., and Soden, B. J.: Clear-sky biases in satellite infrared estimates of upper tropospheric humidity and its trends, *J. Geophys. Res.*, 116, D14108, doi:10.1029/2010JD015355, 2011. 13655, 13658, 13664

John, V. O., Holl, G., Atkinson, N., and Buehler, S. A.: Monitoring scan asymmetry of microwave humidity sounding channels using simultaneous all angle collocations (SAACs), *J. Geophys. Res.-Atmos.*, 118, 1536–1545, doi:10.1002/jgrd.50154, 2013. 13658

Johnston, M. S., Eriksson, P., Eliasson, S., Jones, C. G., Forbes, R. M., and Murtagh, D. P.: The representation of tropical upper tropospheric water in EC Earth V2, *Clim. Dynam.*, 39, 2713–2731, doi:10.1007/s00382-012-1511-0, 2012. 13659

Kirk-Davidoff, D. B., Goody, R. M., and Anderson, J. G.: Analysis of sampling errors for climate monitoring satellites, *J. Climate*, 18, 810–822, doi:10.1175/JCLI-3301.1, 2005. 13656

Liang, C., Eldering, A., Gettelman, A., Tian, B., Wong, S., Fetzer, E., and Liou, K.: Record of tropical interannual variability of temperature and water vapor from a combined AIRS-MLS data set, *J. Geophys. Res.*, 116, D06103, doi:10.1029/2010JD014841, 2011. 13655, 13664

Lin, J.-L., Lee, M.-I., Kim, D., Kang, I.-S., and Frierson, D. M. W.: The impacts of convective parameterization and moisture triggering on AGCM-simulated convectively coupled equatorial waves, *J. Climate*, 21, 883–909, doi:10.1175/2007JCLI1790.1, 2008. 13669

Spatio-temporal impact of convection: methodology

M. S. Johnston et al.

Title Page

Abstract

Introduction

Conclusions

References

Tables

Figures

◀

▶

◀

▶

Back

Close

Full Screen / Esc

Printer-friendly Version

Interactive Discussion



- Loeb, N. G., Wielicki, B. A., Doelling, D. R., Smith, G. L., Keyes, D. F., Kato, S., Manalo-Smith, N., and Wong, T.: Toward optimal closure of the Earth's top-of-atmosphere radiation budget, *J. Climate*, 22, 748–766, doi:10.1175/2008JCLI2637.1, 2009. 13660
- Luo, Z. and Rossow, W. B.: Characterizing tropical cirrus life cycle, evolution, and interaction with upper-tropospheric water vapor using Lagrangian trajectory analysis of satellite observations, *J. Climate*, 17, 4541–4563, 2004. 13665
- Mapes, B. and Houze, R.: Cloud clusters and superclusters over the oceanic warm pool, *Mon. Weather Rev.*, 121, 1398–1416, 1993. 13655, 13665
- Nam, C., Bony, S., Dufresne, J.-L., and Chepfer, H.: The “too few, too bright” tropical low-cloud problem in CMIP5 models, *Geophys. Res. Lett.*, 39, L21801, doi:10.1029/2012GL053421, 2012. 13674
- Nesbitt, S. W. and Zipser, E. J.: The diurnal cycle of rainfall and convective intensity according to three years of TRMM measurements, *J. Climate*, 16, 1456–1475, doi:10.1175/1520-0442-16.10.1456, 2003. 13665
- Qian, Y., Long, C. N., Wang, H., Comstock, J. M., McFarlane, S. A., and Xie, S.: Evaluation of cloud fraction and its radiative effect simulated by IPCC AR4 global models against ARM surface observations, *Atmos. Chem. Phys.*, 12, 1785–1810, doi:10.5194/acp-12-1785-2012, 2012. 13657
- Randall, D. A., Wood, R. A., Bony, S., Colman, R., Fichet, T., Fyfe, J., Kattsov, V., Pitman, A., Shukla, J., Srinivasan, J., Stouffer, R. J., Sumi, A., and Taylor, K. E.: Climate models and their evaluation, in: *Climate Change 2007: The Physical Science Basis. Contribution of Working Group I to the Fourth Assessment Report of the Intergovernmental Panel on Climate Change*, edited by: Solomon, S., Qin, D., Manning, M., Chen, Z., Marquis, M., Averyt, K. B., Tignor, M. and Miller, H. L., Cambridge University Press, Cambridge, UK and New York, NY, USA, 2007. 13656
- Reed, R. J. and Recker, E. E.: Structure and properties of synoptic-scale wave disturbances in the equatorial western Pacific, *J. Atmos. Sci.*, 28, 1117–1133, doi:10.1175/1520-0469(1971)028<1117:SAPOSS>2.0.CO;2, 1971. 13667
- Soden, B. J.: The diurnal cycle of convection, clouds, and water vapor in the tropical upper troposphere, *Geophys. Res. Lett.*, 27, 2173–2176, doi:10.1029/2000GL011436, 2000. 13655
- Soden, B. J.: The impact of tropical convection and cirrus on upper tropospheric humidity: a Lagrangian analysis of satellite measurements, *Geophys. Res. Lett.*, 31, 2333–2351, doi:10.1029/2004GL020980, 2004. 13655, 13665

Spatio-temporal impact of convection: methodology

M. S. Johnston et al.

Title Page

Abstract

Introduction

Conclusions

References

Tables

Figures

◀

▶

◀

▶

Back

Close

Full Screen / Esc

Printer-friendly Version

Interactive Discussion



Stephens, G. L., Vane, D. G., Boain, R. J., Mace, G. G., Sassen, K., Wang, Z., Illingworth, A. J., O'Connor, E. J., Rossow, W. B., Durden, S. L., Miller, S. D., Austin, R. T., Benedetti, A., Mitrescu, C., and the CloudSat Science Team: The CloudSat mission and the A-train, *B. Am. Meteorol. Soc.*, 83, 1771–1790, doi:10.1175/BAMS-83-12-1771, 2002. 13659

5 Stephens, G. L., L'Ecuyer, T., Forbes, R., Gettleman, A., Golaz, J.-C., Bodas-Salcedo, A., Suzuki, K., Gabriel, P., and Haynes, J.: Dreary state of precipitation in global models, *J. Geophys. Res.*, 115, D24211, doi:10.1029/2010JD014532, 2010. 13656, 13666

Tian, B., Soden, B. J., and Wu, X.: Diurnal cycle of convection, clouds, and water vapor in the tropical upper troposphere: satellites versus a general circulation model, *J. Geophys. Res.*, 109, D10101, doi:10.1029/2003JD004117, 2004. 13655

10 Webster, P. J., Clayson, C. A., and Curry, J. A.: Clouds, radiation, and the diurnal cycle of sea surface temperature in the tropical western Pacific, *J. Climate*, 9, 1712–1730, doi:10.1175/1520-0442(1996)009<1712:CRATDC>2.0.CO;2, 1996. 13655

15 Wielicki, B. A., Barkstrom, B. R., Harrison, E. F., Lee, R. B., Smith, G. L., and Cooper, J. E.: Clouds and the Earth's Radiant Energy System CERES: an earth observing system experiment, *B. Am. Meteorol. Soc.*, 77, 853–868, doi:10.1175/1520-0477(1996)077<0853:CATERE>2.0.CO;2, 1996. 13660

Winker, D. M., Hunt, W. H., and McGill, M. J.: Initial performance assessment of CALIOP, *Geophys. Res. Lett.*, 34, L19803, doi:10.1029/2007GL030135, 2007. 13659

20 Wright, J. S., Fu, R., and Heymsfield, A. J.: A statistical analysis of the influence of deep convection on water vapor variability in the tropical upper troposphere, *Atmos. Chem. Phys.*, 9, 5847–5864, doi:10.5194/acp-9-5847-2009, 2009. 13665

Zelinka, M. D. and Hartmann, D. L.: Response of humidity and clouds to tropical deep convection, *J. Climate*, 22, 2389–2404, doi:10.1175/2008JCLI2452.1, 2009. 13655, 13656, 13662

Spatio-temporal impact of convection: methodology

M. S. Johnston et al.

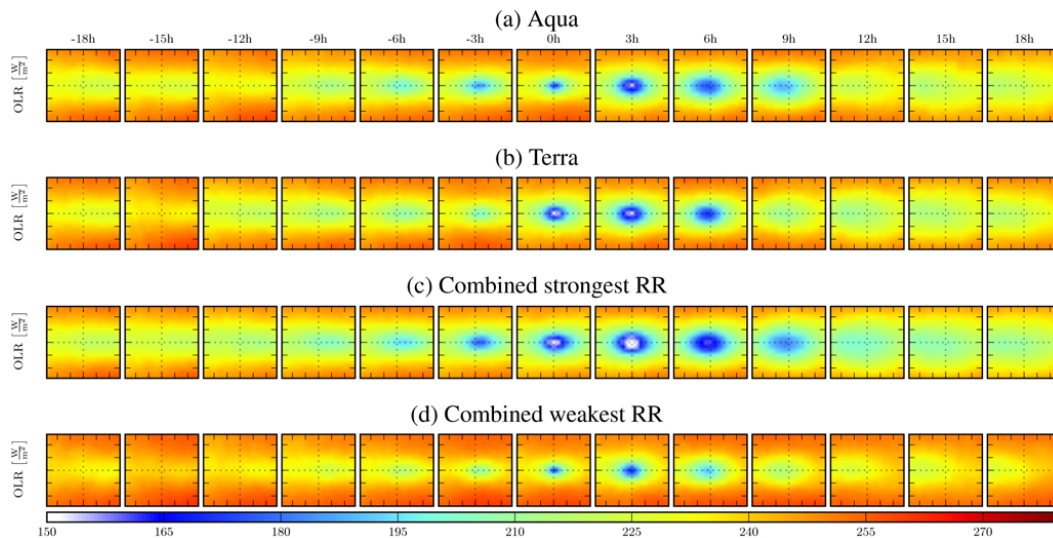


Fig. 1. OLR, averaged as described in Sect. 3.2, from the CERES sensors onboard the sun-synchronous satellites Terra and Aqua. Equatorial passage times for Aqua and Terra are 01:30/13:30 LST (local solar time) and 10:30 L/22:30 LST respectively. Friezes **(a)** and **(b)** show an averaged OLR for all DC events for each sensor separately. In panels **(c)** and **(d)** the two sensors are combined, but the DC events have been divided: frieze **(c)** includes of the top 50 % (21.6 to 70.0 mm h⁻¹) of the 11 000 strongest cases, and frieze **(d)** shows the remainder. The spatial extent of each plot is 12° × 12°.

Title Page

Abstract

Introduction

Conclusions

References

Tables

Figures

◀

▶

◀

▶

Back

Close

Full Screen / Esc

Printer-friendly Version

Interactive Discussion



Spatio-temporal impact of convection: methodology

M. S. Johnston et al.

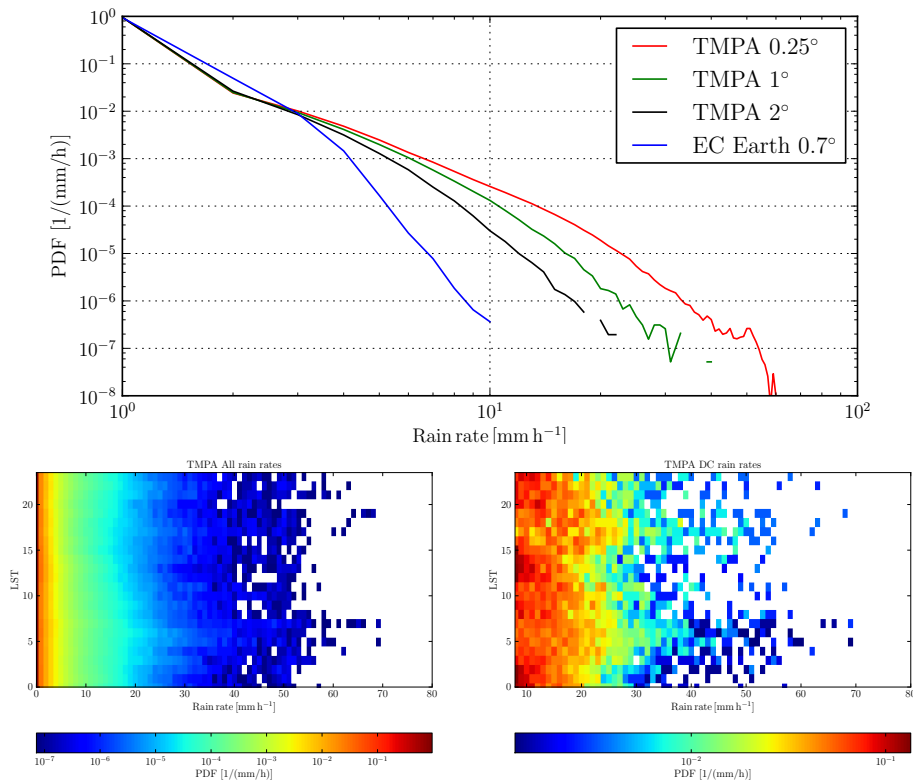


Fig. 2. Probability density functions (PDF) of precipitation over the central Pacific for the period 2007–2008. The top panel shows TMPA at its native resolution (red), resampled to 1° (green) and to 3° (black), and the model (blue). The bottom left panel shows the TMPA probability density per local solar time (LST), while the bottom right panel is the same but includes only the peak RR of the DC events used in this study.

Spatio-temporal impact of convection: methodology

M. S. Johnston et al.

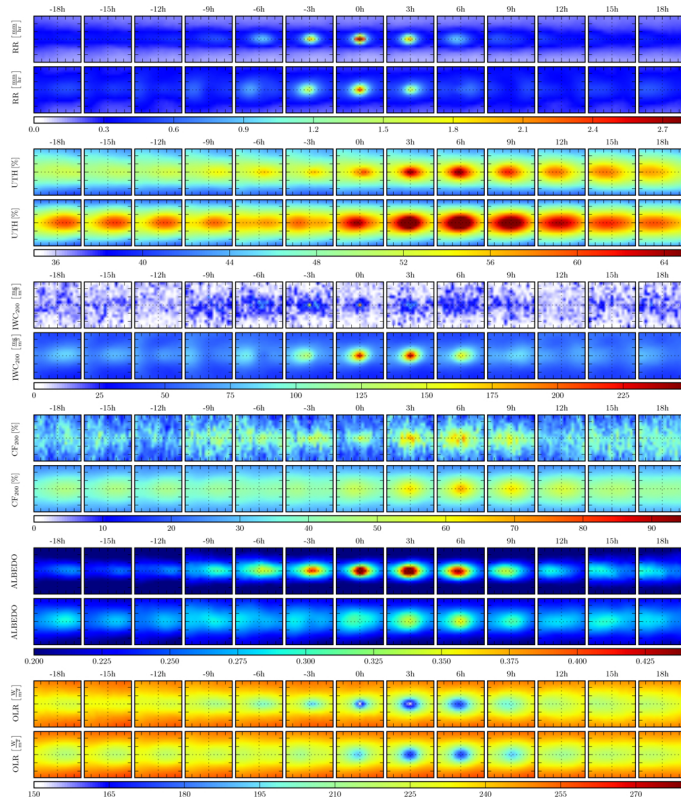


Fig. 3. Time friezes for mean surface rain rate (RR), upper tropospheric humidity (UTH; mean RH_i between 500 and 200 hPa), ice water content (IWC), cloud fraction (CF), albedo, and outgoing longwave radiation (OLR). Cloud fraction and ice water content are shown for 200 hPa. The time bins between ± 18 h are shown and the spatial size of each plot is a $12^\circ \times 12^\circ$ box. For each frieze pair, satellite data averages are found at the top and the corresponding model data is found in the row directly below.

[Title Page](#)
[Abstract](#)
[Introduction](#)
[Conclusions](#)
[References](#)
[Tables](#)
[Figures](#)
[Back](#)
[Close](#)
[Full Screen / Esc](#)
[Printer-friendly Version](#)
[Interactive Discussion](#)


Spatio-temporal impact of convection: methodology

M. S. Johnston et al.

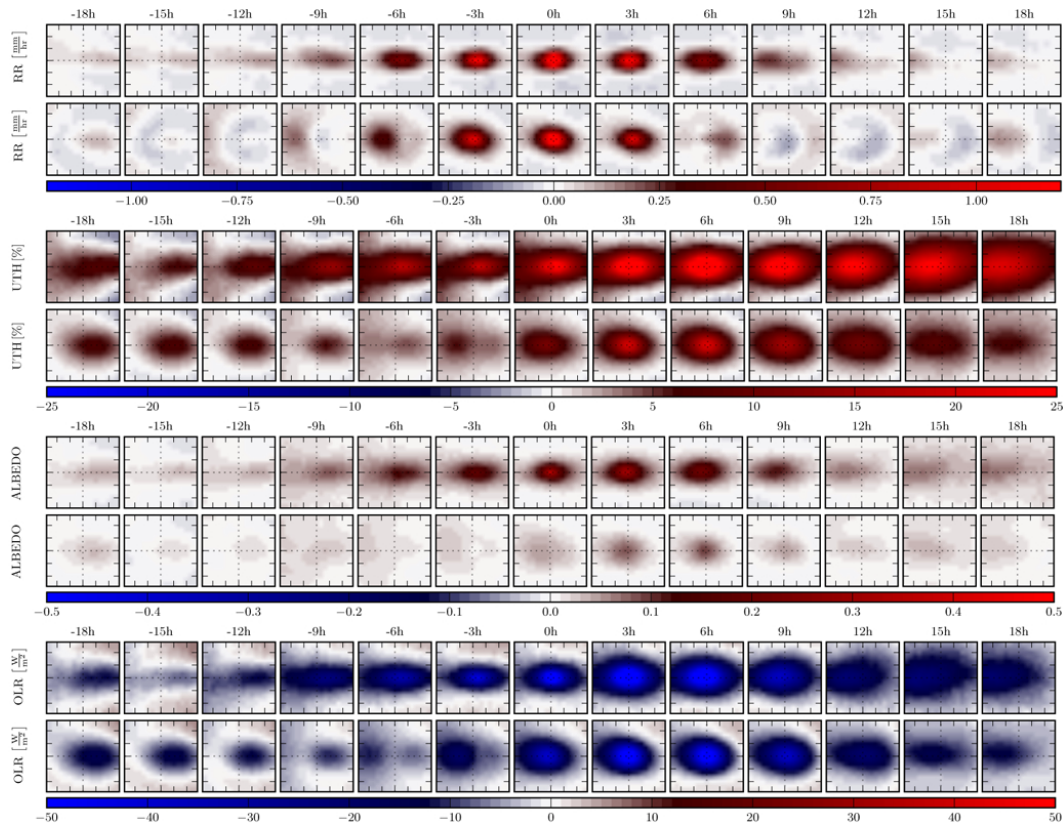


Fig. 4. Anomaly friezes, covering four different variables. The determination of background states is described in the text. The variables are, from the top: surface rain rate (RR), upper tropospheric humidity (UTH; mean RH, between 500 and 200 hPa), and outgoing longwave radiation (OLR). All other aspects of the figure are as Fig. 3.

Spatio-temporal impact of convection: methodology

M. S. Johnston et al.

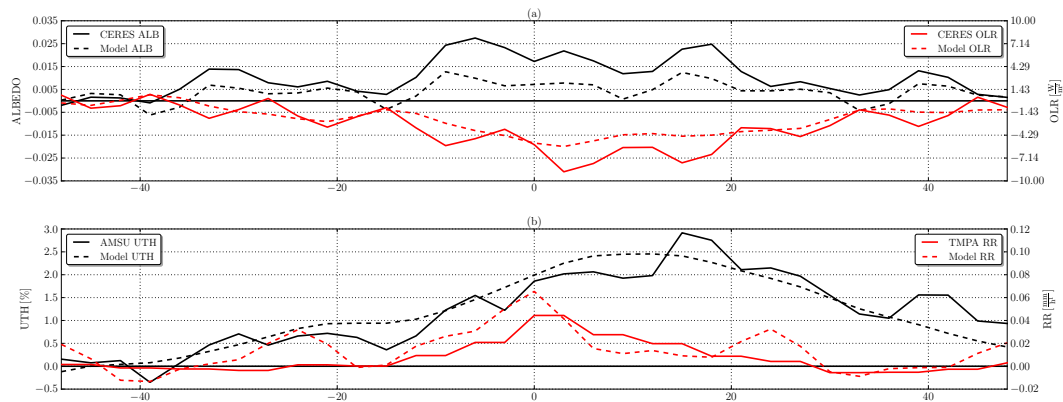


Fig. 5. Spatially averaged responses to deep convection. The averaging is done over 13° latitude and 21° longitude. The background state (i.e. the zero level) is taken as the spatio-temporal average of -48 to -39 h. Solid lines represent satellite observations and dashed lines EC-Earth. The panels show **(a)** albedo and OLR and **(b)** UTH and RR.

[Title Page](#)
[Abstract](#)
[Introduction](#)
[Conclusions](#)
[References](#)
[Tables](#)
[Figures](#)
[◀](#)
[▶](#)
[◀](#)
[▶](#)
[Back](#)
[Close](#)
[Full Screen / Esc](#)
[Printer-friendly Version](#)
[Interactive Discussion](#)


Spatio-temporal
impact of convection:
methodology

M. S. Johnston et al.

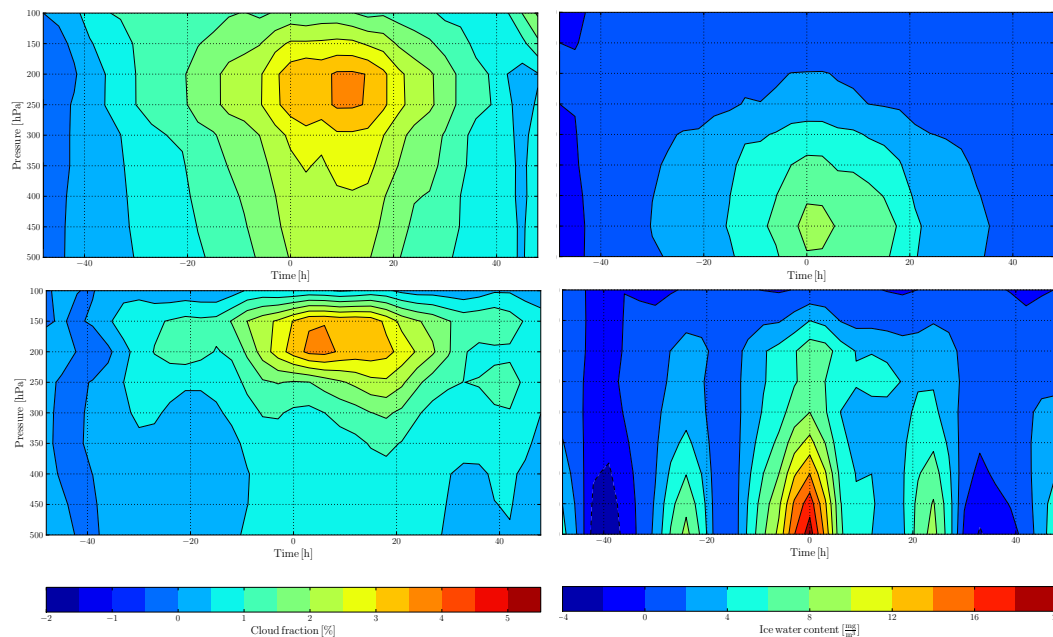


Fig. 6. Vertical variation of spatially averaged anomaly of cloud fraction (left column) and ice water content (right column). The averaging is done over 13° latitude and 21° longitude. The background state is computed in the same manner as Fig. 5. The 2C-ICE dataset is shown in the top row and the model in the bottom. The 2C-ICE plots are smoothed using a moving-average window of 12 h with symmetrical boundary conditions.

[Title Page](#)[Abstract](#)[Introduction](#)[Conclusions](#)[References](#)[Tables](#)[Figures](#)[◀](#)[▶](#)[◀](#)[▶](#)[Back](#)[Close](#)[Full Screen / Esc](#)[Printer-friendly Version](#)[Interactive Discussion](#)